



TECHNOLOGY DEVELOPMENT FOR EXOPLANET MISSIONS

Technology Milestones #1.5, 2.5, and 3 Final Report: Nulling of an Actively-Controlled Segmented Aperture Telescope

Brian Hicks^{1,2} (PI), Michael Helmbrecht³, Peter Petrone^{4,2}, Teresa Sheets², Andrew Lea^{5,2}

¹University of Maryland, College Park, MD

²NASA Goddard Space Flight Center, Greenbelt, MD

³Iris AO, Inc., Berkeley, CA

⁴Sigma Space, Lanham, MD

⁵Stinger Ghaffarian Technologies, Greenbelt, MD

July 20, 2019

National Aeronautics and Space Administration

Jet Propulsion Laboratory
California Institute of Technology
Pasadena, California

Approvals

Released by

Brian Hicks
Principal Investigator

Approved by

Nicholas Siegler
Exoplanet Exploration Program Chief Technologist, NASA JPL

Brendan Crill
Exoplanet Exploration Deputy Program Chief Technologist, NASA JPL

Douglas Hudgins
Exoplanet Exploration Program Scientist, NASA HQ

Contents

1	Project Scope and Milestone Objectives	3
2	System Overview	4
2.1	Radiometry	5
2.2	Controllers and sensors	6
3	Milestones 1.5 and 2.5: Narrowband and Broadband Nulling	7
3.1	Source stability	8
3.2	Chamber stability	9
3.3	Nuller stability	10
3.4	Broadband symmetric transmission optics measurements	11
4	Milestone 3: Broadband Segmented Aperture Nulling	12
4.1	Segmented primary mirror alignment	13
4.2	Fine Pointing System (FPS) performance	14
4.3	Uncontrolled telescope alignment drift and end-to-end jitter	14
4.4	End-to-end operational status and next steps	15
5	Summary	16
	Appendix A: Status of VNC TDEM-13 Whitepaper Needs	17
	Appendix B: Comparison of VNC TDEM-09 and TDEM-13 Hardware	18
	Appendix C: TDEM-13 Subsystem Performance Summary	19
	Appendix D: Segmented Coronagraph Design Analysis (SCDA)	21

Acronyms

APS	Achromatic Phase Shifter
ASF	Aperture Spread Function
ATC	Angle Tracker Camera
BS	Beamsplitter
CPU	Central Processing Unit (generically, “computer”)
DM	Deformable Mirror
FPS	Fine Pointing System
FSM	Fast Steering Mirror
FWHM	Full Width at Half Maximum
IWA	Inner Working Angle
LOWFS	Low-Order Wavefront Sensor
MMA	Multiple Mirror Array, a.k.a. (hex-packed) segmented DM
MS	Milestone
PSF	Point Spread Function
PTT	Piston–Tip–Tilt (or piston, tip, and tilt)
PZT	PieZoelectric Transducer (or “piezo”)
RMS	Root Mean Square
SAT	Strategic Astrophysics Technology
SAINT	Segmented Aperture Interferometric Interferometric Nulling Testbed
SCDA	Segmented Coronagraph Design Analysis
TDEM	Technology Development for Exoplanet Missions
TRL	Technology Readiness Level
VNC	Visible Nulling Coronagraph
WFS	Wavefront Sensor
WFS/C	Wavefront Sensing and Control
WFE	Wavefront Error

1 Project Scope and Milestone Objectives

Major breakthroughs in exoplanet science and discovery will be enabled by high-contrast direct imaging detection and spectroscopic characterization of the atmospheres of habitable worlds orbiting mature, quiescent, and nearby stars. The space telescopes that will make these observations will need to be large to address exoplanet direct imaging resolution and photometric flux constraints, and it is reasonable to expect that these telescopes will build upon hexagonal array segmented mirror infrastructure in order to fit inside of limited launch fairing volumes. Sensitivity to any existing Earth-like planets orbiting the many hundreds of nearest stars may be achieved by pairing an adequately-sized telescope with a coronagraphic starlight suppression system having active optical wavefront sensing and control (WFS/C) elements to correct for optical scattering. Controlling optical elements in these systems to find and hold an alignment solution at unprecedented levels of precision in the presence of dynamic perturbations presents a formidable challenge for increasingly complex laboratory experiments striving towards higher fidelity demonstrations.

In support of NASA's Exoplanet Exploration Program and the Technology Development for Exoplanet Missions (TDEM)[1] component of NASA's Strategic Astrophysics Technology (SAT) program, the Visible Nulling Coronagraph (VNC) at NASA's Goddard Space Flight Center has been coupled with an actively-controlled macro-scale segmented primary mirror via a fine pointing system (FPS) to form the Segmented Aperture Interferometric Nulling Testbed (SAINT).[2, 3, 4] SAINT has been developed to date as an end-to-end coronagraphic system to demonstrate high-contrast WFS/C imaging in the presence of complex diffraction and environmental instabilities with traceability to future large space telescopes having coronagraphic high-contrast imaging capability.

A first Milestone goal for this TDEM-13 effort (MS 1.5) included reproducing or exceeding earlier VNC narrowband performance achieved in the TDEM-09 program. This specific objective entails achieving and repeating mean contrast of at least 10^{-8} at a $2\lambda/D$ inner working angle (IWA) measured over a circular region spanning $1.5\lambda/D$ to $2.5\lambda/D$ at a visible wavelength centered in a narrowband filter of spectral bandpass $< 1\%$ for 1,000 seconds on three separate occasions.[5, 6]

A second Milestone goal for this TDEM-13 effort (MS 2.5) was to achieve a mean contrast metric of 1×10^{-9} over the same region as MS 1(.5), but using a spectral filter of 40 nm FWHM, and once again demonstrating repeat performance on three second occasions.[7, 8, 9, 10]

This TDEM-13 program's final Milestone (MS 3) objective comprised holding a contrast of 10^{-8} at an IWA of $4\lambda/D$ within a bandpass of $\Delta\lambda = 20\text{nm}$ centered near 633nm for 1,000 seconds on three separate occasions, with a goal of 10^{-9} at an IWA of $3\lambda/D$ over a $\Delta\lambda = 40\text{nm}$ bandpass. Satisfying these MS objectives remain the next steps in establishing the VNC as a viable option for a future large space telescope requiring capability for directly detecting and characterizing Earth-like exoplanets.

No best-achieved contrast is provided for the standalone VNC due to a lack of success closing the loop on wavefront control, therefore no best-achieved contrast is provided for SAINT. Having not successfully met MS objectives in this effort, this TDEM-13 Final Report presents the operational status of the telescope, pointing, and coronagraph component subsystems, including a demonstration of end-to-end SAINT system basic operation achieved in early 2018.

2 System Overview

SAINT was developed to meet VNC TDEM-13 MS 3 objectives. This report adds detail to the incremental descriptions of the VNC (§3 below, [6] §2.1, and [10] §2) and SAINT systems (§4) published in recent years.[2, 9, 3, 4] SAINT pairs the VNC operating in a vacuum chamber with an actively-controlled segmented telescope that is housed in an enclosure. The chamber provides an isolated environment for demonstrations at atmospheric pressure and pressures relevant to high-altitude and space platforms. The vacuum chamber rests atop a passively stabilized air table that supports the full system. Vacuum feedthroughs consisting of electrical cables and water chiller lines to cool the high-contrast focal plane detector pass through multiple tank bulkheads. Fig. 1 shows a raytrace of the end-to-end high-contrast paths, and system pupil geometries and corresponding aperture spread function (ASF) plots are shown in Fig. 2. The telescope optics form one of two selectable source inputs for the VNC, the other being a circular aperture with Gaussian intensity profile for intermediate MS 1.5 narrowband and broadband MS 2.5 demonstrations of the VNC alone.

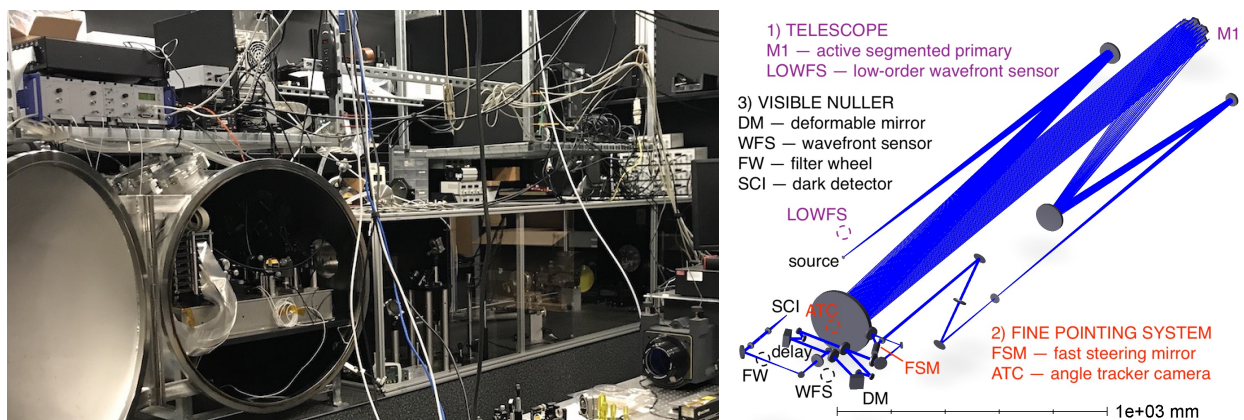


Figure 1: The SAINT system and raytrace showing the end-to-end system path and locations of subsystems, sensing, and control components. In addition to the labeled components, each arm of the VNC has a shutter that can be closed to calibrate imaging quality, measure source brightness fluctuations, as well as to measure and balance intensities on the high contrast detector in the dark, symmetric output of the nuller.

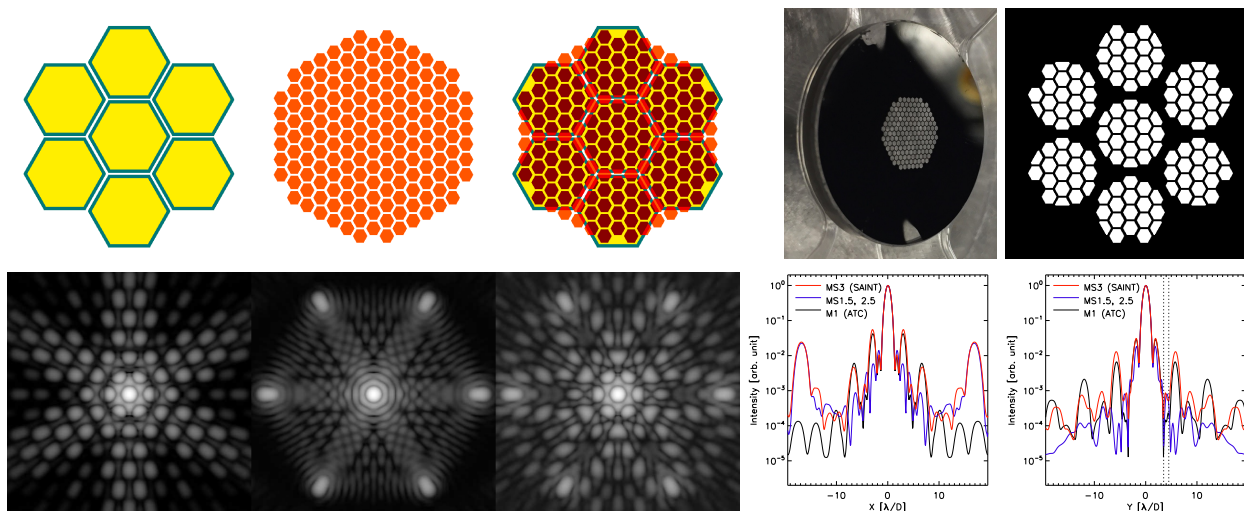


Figure 2: VNC TDEM-13 MS 1.5, 2.5 and 3 pupil geometries, masks, and logarithmically stretched ASFs. The intersection of the telescope primary and deformable mirror define the SAINT exit pupil. The upper right physical and digital masks were presented together in 2017. The lower panels plot slices through the ASF centers, and vertical dashed lines highlight the bounds on the MS 3 high-contrast region.[3]

2.1 Radiometry

The SAINT end-to-end optical path traverses 36 elements and 51 Fresnel interfaces when accounting for only a single arm of the nuller, and 43 elements and 64 interfaces for both the delay stage and deformable mirror (DM) arms. It remains an objective to achieve a further reduction in the number of elements and interfaces through, e.g., optical contracting and merging fold mirrors and lenses into custom off-axis mirrors. Fewer optics are traversed to reach the other detectors in the system.

VNC (MS1.5 & MS2.5)				SAINT (MS3)								
source	1.000			source	1.00							
fiber	0.600	0.60000		collimator M2	0.50	0.50000						
lens	0.970	0.58200		telescope M2	0.97	0.48500						
lens	0.970	0.56454		fold	0.97	0.47045						
stop	0.600	0.33872		sampler	0.96	0.45163	sampler	0.040	0.01882			
polarizer	0.980	0.33195		periscope	0.97	0.43808	periscope	0.970	0.01825			
fold	0.970	0.32199		lens	0.98	0.42932	fold	0.970	0.01771			
fold	0.970	0.31233		periscope	0.97	0.41644	lens	0.980	0.01735			
lens	0.980	0.30608		window	0.98	0.40811	fold	0.970	0.01683			
50/50	0.450	0.13774		lens	0.98	0.39995	lens	0.420	0.00707			
polarier	0.900	0.12396		FSM	0.97	0.38795	LOWFS	0.720	0.00509			
fold	0.970	0.12025		R=0.9 T=0.1	0.90	0.34916	R=0.9 T=0.1	0.100	0.03880			
fold	0.970	0.11664		polarizer	0.98	0.34217	fold	0.970	0.03763			
fold/DM	0.970	0.11314		fold	0.97	0.33191	lens	0.980	0.03688			
APS	0.995	0.11257		fold	0.97	0.32195	fold	0.970	0.03577			
50/50 (x 2)	0.450	0.10132	50/50	0.450	0.05066		lens	0.98	0.31551	ATC	0.500	0.01789
fold	0.970	0.09828	fold	0.970	0.04914		50/50	0.45	0.28396			
lens	0.980	0.09631	fold	0.970	0.04766		polarier	0.90	0.25556			
fold	0.970	0.09342	lens	0.980	0.04671		fold	0.97	0.24790			
MS 1.5 filter	0.003	0.00023	WFS	0.650	0.03036		fold	0.97	0.24046			
lens	0.980	0.00023					fold/DM	0.97	0.23325			
mask	0.541	0.00013					APS	1.00	0.23208			
fold	0.970	0.00012					50/50	0.45	0.10444	50/50	0.450	0.10444
fold	0.970	0.00012					fold	0.97	0.10130	fold	0.970	0.10130
barlow	0.900	0.00011					lens	0.98	0.09928	fold	0.970	0.09826
SCI	0.570	0.00006					fold	0.97	0.09630	lens	0.980	0.09630
MS 2.5 filter	0.100	0.00934					MS 3 filter	0.05	0.00481	WFS	0.650	0.06259
lens	0.980	0.00916					lens	0.98	0.00472			
mask	0.541	0.00495					mask	0.54	0.00255			
fold	0.970	0.00481					fold	0.97	0.00248			
fold	0.970	0.00466					fold	0.97	0.00240			
barlow	0.900	0.00419					barlow	0.90	0.00216			
SCI	0.570	0.00239					SCI	0.57	0.00123			

Table 1: Approximate transmission and relative beam power following the traversal of each optic for all three TDEM-13 MS configurations. Solid horizontal lines denote locations where the beam is sampled or split and diverted for each WFS/C subsystem. For MS 1.5 and 2.5, a dashed line indicates a breakpoint and flowdown from the narrow- and broadband intermediate MS filters. The ratios of end-to-end SAINT (MS 3) and VNC (MS 1.5 and 2.5) throughput are consistent with the ratios of exposure times and intensities presented in Tab. 2 and Fig. 3

Source brightness, system transmission, diffraction, aberrations, coatings and surface errors, magnification, as well as detector dynamic range and noise all play a role in determining control rates and the number of exposures required to measure an arbitrary scattered light residual with arbitrary confidence for a given detector over a given bandpass. Tab. 2 and Fig. 3 present characteristics of the VNC intermediate narrowband and broadband MS 1.5 and MS 2.5 filters, respectively, as well as the SAINT final end-to-end MS 3 filter. The central wavelength, λ , and full-width at half-maximum (FWHM) for each filter were previously measured using a spectrophotometer.[10]

Table 2: VNC/SAINT imaging bandpass characteristics corresponding to Fig. 3

filter	λ (nm)	FWHM (nm)	$\Delta\lambda/\lambda$ (%)	$\lambda^2/\Delta\lambda$ (waves)	τ (ms)	rate (fps)
MS 1.5	632.8	1.26	0.20	502	2.00	45
MS 2.5	654.7	31.7	4.84	21	0.25	50
MS 3	649.2	17.5	2.70	37	0.25	50

Figure 3 shows cross-sections through the point spread function (PSF) observed by the VNC dark detector under both faint source and high background, as well as bright source, low background conditions, using each of the two intermediate and final MS filters. As expected, off-axis pixel intensities are observed to increase with longer integration of dark current and background. The dashed lines correspond to the contrast measurement critical boundaries for MS 1.5 and 2.5, and the dashed-dotted lines correspond to the MS 3 critical boundaries. The ratio of core to sidelobe intensities can be measured and used to increase the maximum contrast in a single frame. To illustrate this, the exposure times were set for the Milestone 1.5 filter such that the core does not saturate in either the faint or bright source conditions.

For each bandpass, the measured peak intensity is between one and two orders of magnitude greater than the intensity measured in the off-axis range critical to the Milestone demonstrations. Under the condition of destructive interference, the exposure times can be increased to improve the scattered light signal residual,

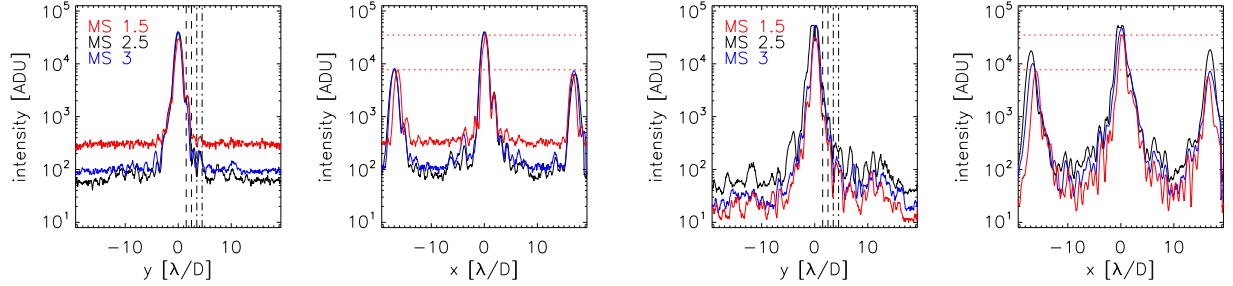


Figure 3: *Left*: PSF cross-sections observed with the VNC dark detector under faint source and dim lab background conditions. *Right*: the same, but under bright source, dark chamber, low background, demonstration-like conditions using exposure times listed in Tab. 2. The MS 2.5 and MS 3 PSF cores are saturated. The PSFs correspond to that of the monochromatic ASF shown in the middle of the lower left panel of Fig. 2.

but only to the limit where perturbations above the resultant maximum control sampling frequency do not exceed the root mean square (RMS) wavefront error (WFE) requirement.

In tentative final contrast demonstrations, the VNC will be operated in vacuum using a single mode fiber feedthrough that has a cutoff wavelength in the range of 500-600nm. The bright source exposure times, τ , and frame rates presented in Tab. 2 were measured by free space coupling a collimated supercontinuum source output to a step index single mode fiber patch cable serving as the VNC input.

2.2 Controllers and sensors

Representative VNC TDEM-13 control software and detector display frames are shown in Fig. 4, and sensors used in the effort are listed in Tab. 3. The computer (CPU) interface and software control development for the full system is distributed between three workstations, all running the same Linux OS.

The first CPU interfaces the SAINT M1 low-order wavefront sensor (LOWFS) detector & wavefront control in the form of rigid body piston/tip/tilt (PTT) actuation of segments via 3-axis piezoelectric transducer (“piezo” or PZT) mounts (see §4.1). The second CPU interfaces the FPS fast steering mirror (FSM) amplifiers for the tip-tilt PZT stage and readout for strain gauge sensors, providing closed-loop displacement feedback for each

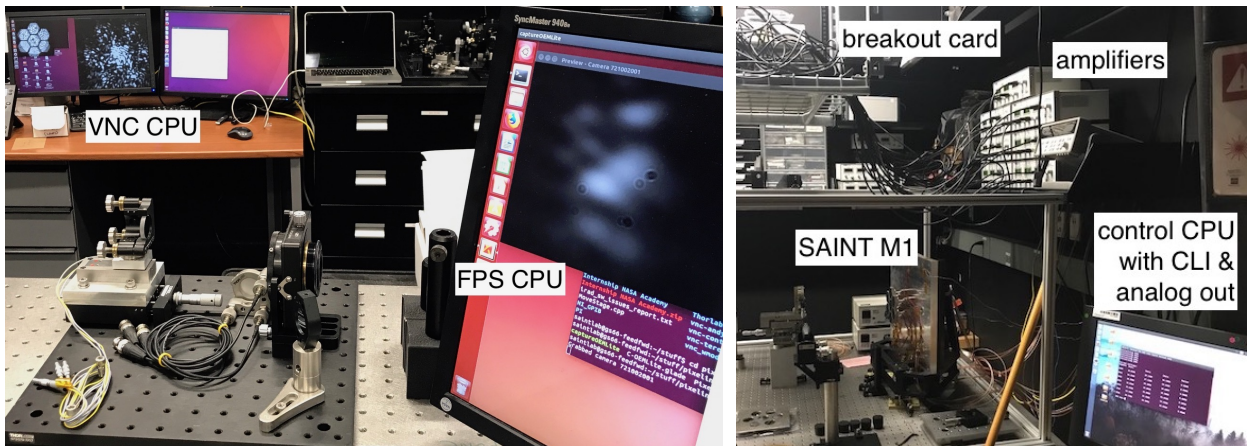


Figure 4: *Left*: Detector displays showing SAINT M1 alignment at power up as viewed by the WFC, SCI, (VNC CPU) and ATC detectors (FPS CPU). *Right*: (from [3]) the hardware and controls comprising the SAINT actively-controlled segmented M1, including control computer with a multichannel analog output PCI card connected to a breakout card that relays to the segment control voltage amplifiers.

axis, as well as an angle tracker camera (ATC) to close the loop on stabilizing pointing jitter (see §4.2). The third CPU commands and reads out components of the VNC including the DM, shutters, delay stage, the “dark” channel high-contrast science detector (SCI), and the high-order “bright” channel wavefront sensor (WFS) referenced in the following §3 and throughout this report.

Table 3: VNC TDEM-13 Detectors

detector	vendor and model	QE ₆₃₃ (%)	dynamic range (-bit)	frame size (pix x pix)	pixel size ($\mu\text{m} \times \mu\text{m}$)	plate scale ($\lambda/D \text{ pix}^{-1}$)
LOWFS	Andor Zyla 4.2	70	16	512 x 512	6.2 x 6.2	0.508
ATC	PixelINK PL-D721MU	50	10	256 x 256	4.8 x 4.8	0.05937
WFS	PixelINK PL-D752MU	65	12	512 x 512	5.9 x 5.9	–
SCI	Andor Neo 5.5	57	16	512 x 512	6.5 x 6.5	0.07573

3 Milestones 1.5 and 2.5: Narrowband and Broadband Nulling

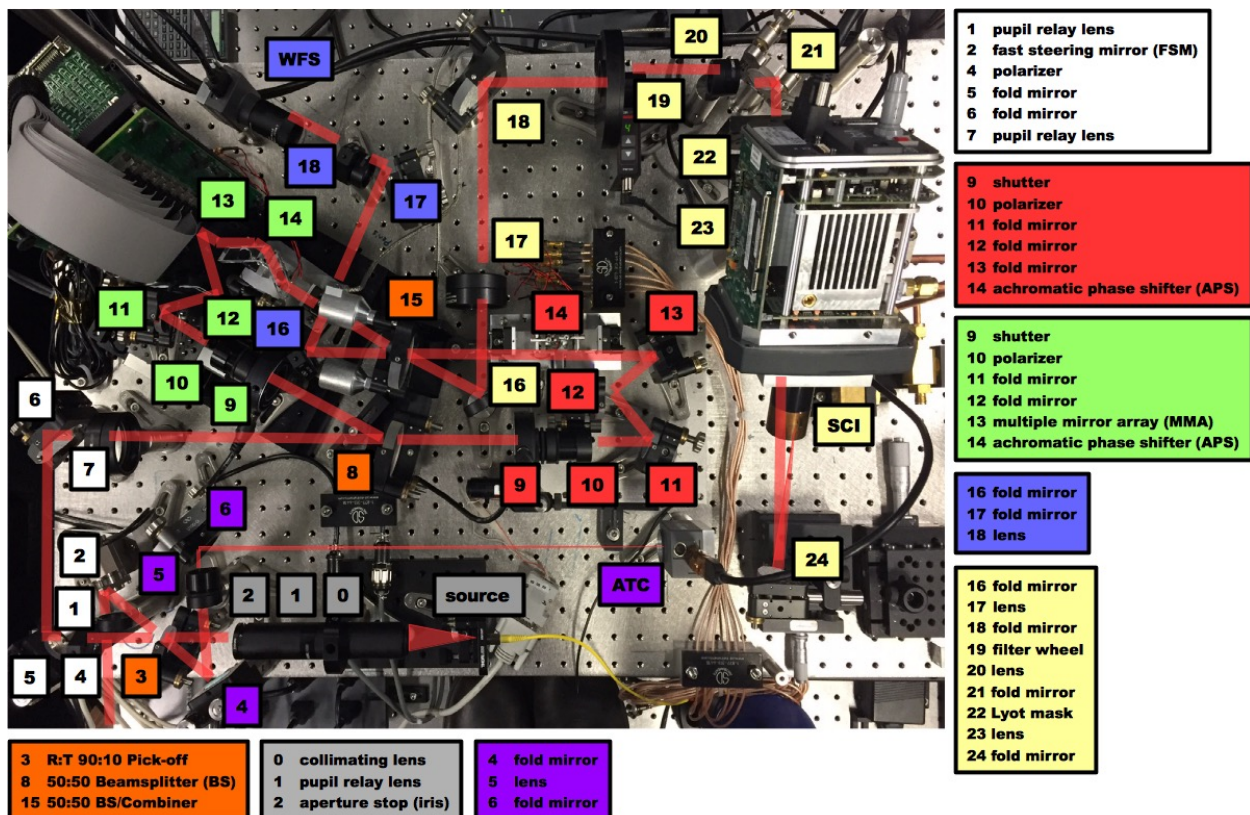


Figure 5: The VNC breadboard (from [3]) including: a compacted source module (*grey*), multiple mirror array (MMA) Iris AO PTT489 segmented DM (*green*) and upgraded delay stage (*red*) interferometer arms, the FPS optics (*purple*) to couple the VNC to the active segmented telescope (§4), and aft-optics (*yellow*) including the bandpass filters that were moved to the destructive “dark” high-contrast output to allow constant tracking of the full source bandpass central broadband constructive fringe with the “bright” output wavefront sensor (WFS) optics (*blue*). Appendix B lists hardware changes relative to the TDEM-09 VNC.

A description of the VNC is presented in previous works.[6, 7, 9] The VNC MS 1 effort (TDEM-9) successfully demonstrated better than 10^{-8} contrast for a $< 1\%$ bandwidth over a $1\lambda/D$ diameter circular area centered at $2\lambda/D$ off-axis from the PSF center.[5, 6] The VNC MS 2 effort (TDEM-10) was unsuccessful in demonstrating

the targeted 10^{-9} contrast over a 4.84% bandwidth in the same region of targeted contrast.[10] This TDEM-13 effort was unsuccessful in its attempts to repeat narrowband MS 1 performance as MS 1.5, and it was unsuccessful in reaching for the first time the broadband MS 2 performance goal recast as MS 2.5.

This section presents measurements recorded with the VNC in a standalone configuration similar to TDEM-9 and TDEM-10 with a single mode fiber source emanating from a fixed point, mounted on the nuller breadboard inside a closed vacuum chamber at atmospheric pressure and room temperature. The VNC as tested in this effort with 2016 upgrades including aft optics, detectors, and delays stage, is shown in Fig. 5. Relevant measurements and analyses in the following Secs. 3.1, 3.2, and 3.3 were presented in a recent work.[4]

3.1 Source stability

The “dark” focal plane SCI detector was used to monitor source stability with the reference arm shutter open and the DM arm shutter closed. These same data were used to quantify mechanical stability (see §3.2). Representative frames for these stability data are labeled in Fig. 6. The first frame in the series is taken to be the reference, which is shown subtracted from the average of all frames in the series. The VNC PSF core and sidelobe diameters and separations are characteristic of the deformable mirror 7-ring hexagonal array and corresponding Lyot mask’s pitch and hole diameters.[5, 6, 11] The sidelobe centers are spaced 60° at a radial distance of $16.166\lambda/D$ from the core center, giving a plate scale of $0.07573\lambda/D$ per pixel.

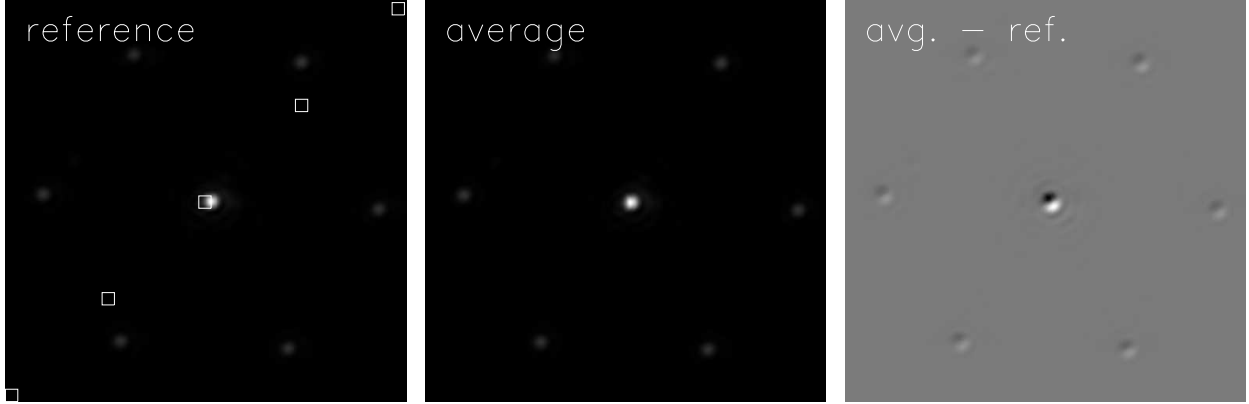


Figure 6: Representative standalone VNC 512×512 pixel SCI detector frames for the time series and power spectra presented in Figs. 7– 9. The five boxes and their centers contain the pixels used in central single pixel and multiple pixel average time series and power spectra.

The time series and power spectra of the data set’s full frame measured intensity statistics are presented in Fig.7. The data set comprises a total of 1000 frames saved at an average rate of 18.52 per second. The power spectrum of the frame maximum series corresponds to $1/f$ noise greater than 0.3Hz.

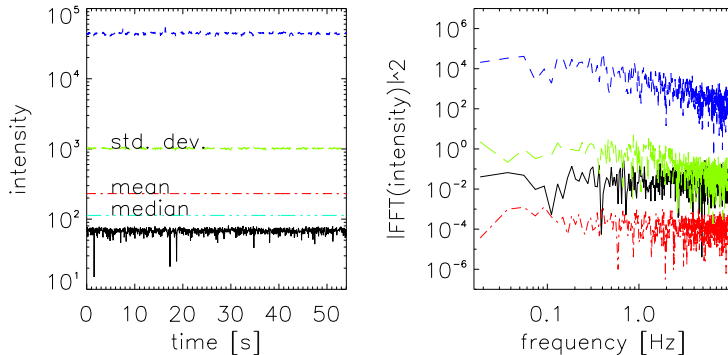


Figure 7: Whole image series statistics including the minimum, maximum, mean, median, and standard deviation for each frame of single arm VNC data under bright source and low background conditions. The maximum pixel value mean and RMS variation over the field of view are 44159.8 and 1471.25 ADU, respectively. The mean and RMS values of the frame mean time series is 230.910 and 0.437117 ADU, respectively.

Effects attributed to fluctuating source uniformity are presented in the time series and power spectra shown in Fig. 7. These time series correspond to five equally spaced individual pixels, as well as approximately $1\lambda/D$ square box averages around these pixels (shown to scale) located along a diagonal in Fig. 6. The measured signal residual in the wings of the PSF approaching the off-axis radial separation of the side lobes and in the corners of the frames is less than 10σ above the detector bias signal. The intensity power spectra are white for individual pixels at all locations except near the core where the spectrum is pink, and pink at all locations for the box averages.

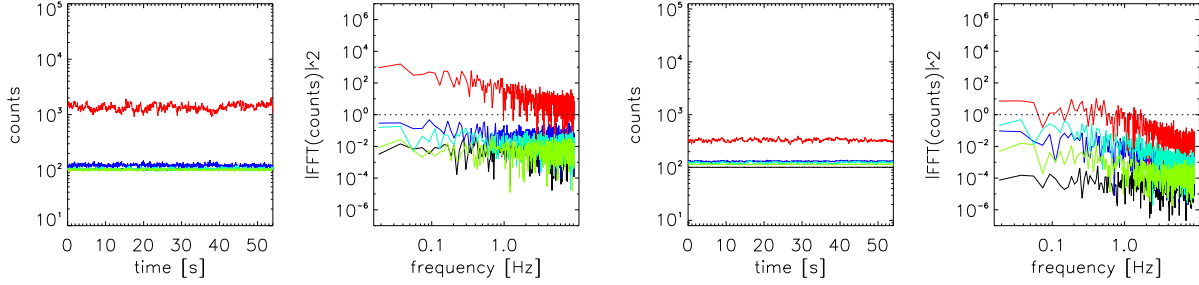


Figure 8: Time series and power spectra for the VNC delay reference arm measured under bright source and low background conditions at single pixel (*left*) and box-averaged (*right*) zones identified in Fig. 7.

3.2 Chamber stability

Here we analyze plots of centroid jitter time series and power spectra for the same VNC single arm data analyzed in §3.1 as a proxy for all effects internal to the chamber that are not attributed to nuller path length fluctuations. The PSF core spans several pixels, and Fig. 6 reveals drift across typically less than three pixels ($< 0.23\lambda/D$) over several tens of seconds. Experimentation at different magnifications under otherwise identical conditions might reveal what fraction of the observed spectrum can be attributed to

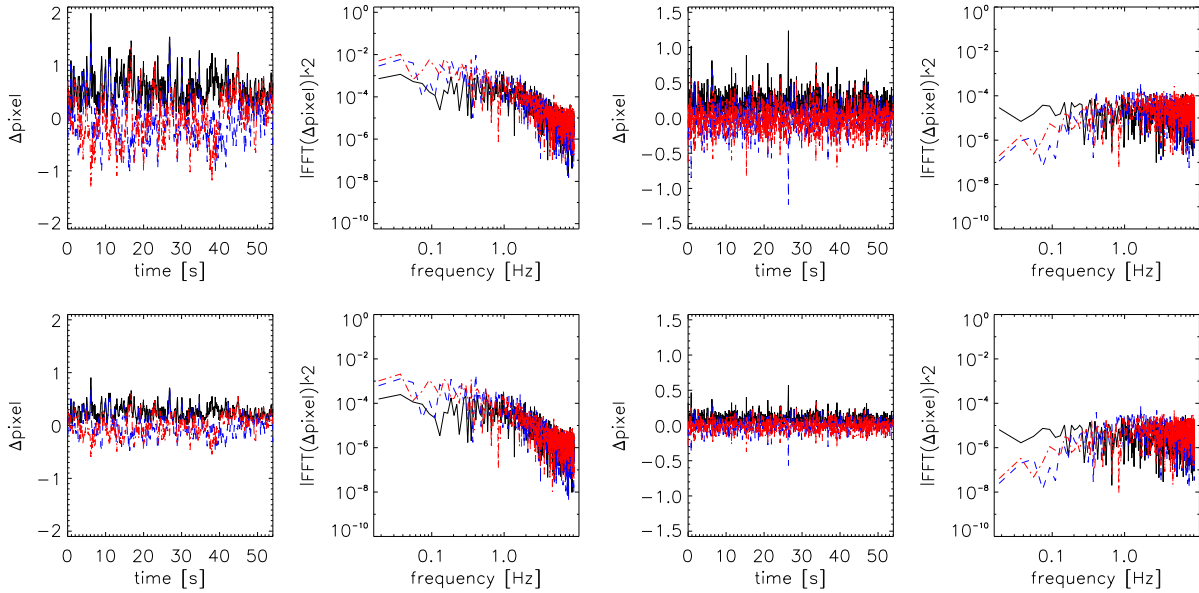


Figure 9: Single arm VNC centroid jitter time series and power spectra plotted for both x and y directions, as well as magnitude relative to the mean centroid location (*top*), and previous frame instantaneous centroid motion (*bottom*).

aliasing at pixel active area scales. Jitter plots are presented in Fig.9 as absolute motion, Δ_{pixel} , in the focal plane relative to the mean frame centroid as a reference (top row), and as instantaneous frame by frame motion (bottom row). The left plots are made from the raw frames, and the right plots are the same data reanalyzed following numerically shifting each frame by fractional pixel centroid offsets in both the absolute and instantaneous treatments to emulate effects of residual errors following pointing correction. Orthogonal jitter components are plotted as dashed and dashed-dotted lines in blue and red, respectively, and the magnitude of the jitter is plotted as a solid black line. The RMS jitter calculated from the raw and shifted data residual relative to the average frame is 0.798 and 0.168 pixels, respectively. For the instantaneous treatment, the offset and residuals are 0.131 and 0.033 pixels RMS. The first frame reference treatment reduces the RMS centroid jitter by 4.75 times, whereas the instantaneous treatment reduces the error by 3.97 times, and ultimately achieves an error that less than 20% of the error achieved referencing relative to the average of all frames.

3.3 Nuller stability

The preceding sections present stability measurements of the VNC encompassing effects excluding phase variability attributed to effects such as differential dispersion and electromechanism stability. Directly compensating for these effects, high-contrast coronagraphic nulling wavefront control step sizes and achievable bandwidth must be significant and fast enough to keep up with measured instabilities while gradually reducing WFE. Here we present and analyze measured stability time series and power spectra similar to what is shown in Fig. 8, but for the case of operating near a destructive interferometric null. Time series are measured at the same five image locations in as shown in Fig. 10, and similar to the single arm measurements, both multipixel box averages as well as single pixel intensity time series and power spectra are plotted.

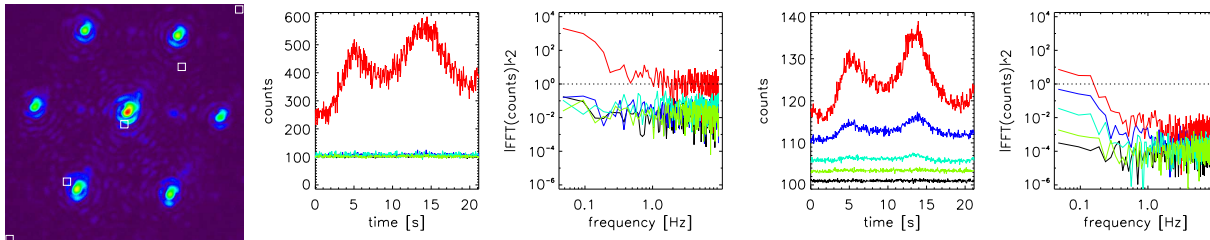


Figure 10: Example interferometric null first frame (*left*) next to its corresponding time series and power spectra for individual pixels centered in each of the five indicated box locations (*center*), and (*right*) time series and power spectra averaged over all pixels in each box. This is the worst case of four such data sets presented in a recent work.[4]

The plots in Fig. 10 convey both the advantage if not also a clear necessity of measuring signal residuals over many pixels, as well as identifying the time scales at which control systems must run in order to address both piston and higher spatial frequency drifts. In the case of ideal optics (no surface errors and uniform dispersion), controlling piston alone to achieve zero optical path difference would suppress the entire PSF in the interferometric dark output, moving all on-axis source light from a point source into the interferometric bright output. It is the higher spatial frequency geometric and coating errors in the optics that scatter and necessitate wavefront correction with DMs targeting a limited region of influence in the focal plane.

The VNC’s control algorithm targets a nearly 60° wedged region of interest that extends radially from 1.5 and $4.5\lambda/D$ for a total of approximately 1000 pixels spanning multiple speckles. Averaging over the region reduces measured detector noise by $n^{1/2}$. Variations in the total or average intensity measured over the full detector region of interest may be fed back to the delay stage to stabilize the piston error, which can be sensed with 0.5nm precision according to specifications. Transverse speckle motion is associated with all spatial frequencies greater than pure piston that can be suppressed by the DM, which is controlled using “mode” patterns that may be ordered according to their influence in the targeted dark zone.[5, 6]

For the data and plots in Fig.10, one of the boxes is located near $\sim 2\lambda/D$ and has an incoherent peak

intensity of 3000 counts. The largest single pixel long period intensity drifts in this region are shown at the ~ 300 to 600 count level, which corresponds to $\lambda/20$ to $\lambda/10$ WFE. The equivalent delay line positional error in the VNC would be about 15 to 30nm. Introducing 1nm controlled perturbations of the DM in a pure piston mode, inserted into the greater control mode scheme at a frequency no lower than 2Hz has been tested with promising results. Introducing a fringe tracking control layer to drive the delay line at higher frequencies could prove to be more efficient overall, and it would eliminate the risk of exceeding the range of linear operation of the DM.

In practice, for both DM and delay control layers, a control step must be large enough such that the resulting measured signal derivative has a high chance of directing a next step in the right direction. When approaching a fringe minimum inflection point, some step size must be chosen in order to reliably indicate the presence of the inflection. The required step size is a function of the noise properties as well as the instantaneous contrast. To the extent that the noise can be decreased by integration, a combination of both appropriate step size and integration time must be chosen. The integration time must also be small enough such that temporal stability timescales do not compromise the measurement. Ultimately, the mode amplitude to detector signal response can be measured in the control loop, and the optimal system automates control amplitude and detector exposure time adjustments.

Convection due to detectors heating the air inside the chamber is suspected as being the greatest contributor to observed fluctuations, and to a lesser extent, acoustic and mechanical motions, as well as source brightness fluctuations. Running the system under a low pressure condition and removing the optical table isolation are two conditions under which data would be collected once routine reliable performance is achieved with the control-loop, and the limit to in-air performance has been established with high confidence. Ultimately, the TDEM-13 project schedule was consumed prior to being able to perform nulling stability measurements in reduced pressure to confirm the significance of convection effects.

3.4 Broadband symmetric transmission optics measurements

A key to achieving broadband destructive interference at high contrast is maintaining transmission symmetry between interfering beams. Fringe offsets were observed and recorded in a Michelson interferometer setup shown in Fig. 11 to measure the difference in optical path thickness for paired transmission optics including achromatic phase shifters (APS) and polarizers. In a successful step toward meeting MS 2.5 broadband performance goals, we successfully acquired, measured, selected and installed polarizers that reduced 79.5 μm TDEM-9 and TDEM-10 polarizer path error to $< 0.1\mu\text{m}$, effectively improving the broadband contrast limit from 10^5 to 10^9 . APS with better matched optical thickness than those designed, acquired, and installed in the VNC for TDEM-10 were received, but several technical¹ delays consumed project schedule prior to mounting the APS to be measured then installed in the VNC.

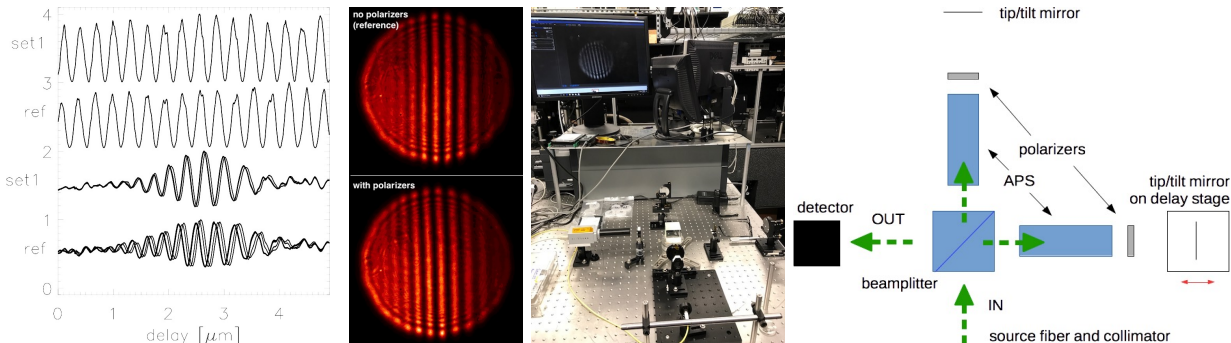


Figure 11: Data and Michelson interferometer used to measure transmissive optical thicknesses critical to MS 2.5. The “ref” plots correspond to having no optics in the Michelson. Repeated measurements are shown for the polarizer pair that was selected for the demonstration effort. Path length variability is attributed to motions in the ambient lab environment. Laser light fringes shown in the top left panel are used for calibration.

4 Milestone 3: Broadband Segmented Aperture Nulling

First light through the SAINT source to VNC dark detector as collected on May 1, 2018 is presented in Fig. 12. The top of Fig. 12 shows typical frames recorded by the WFS, which is unfiltered to achieve the minimum possible coherence length and maximize sensitivity to optical path errors near the central fringe. Columns from left to right in Fig. 12 correspond to closing shutters alternately to allow light to pass through

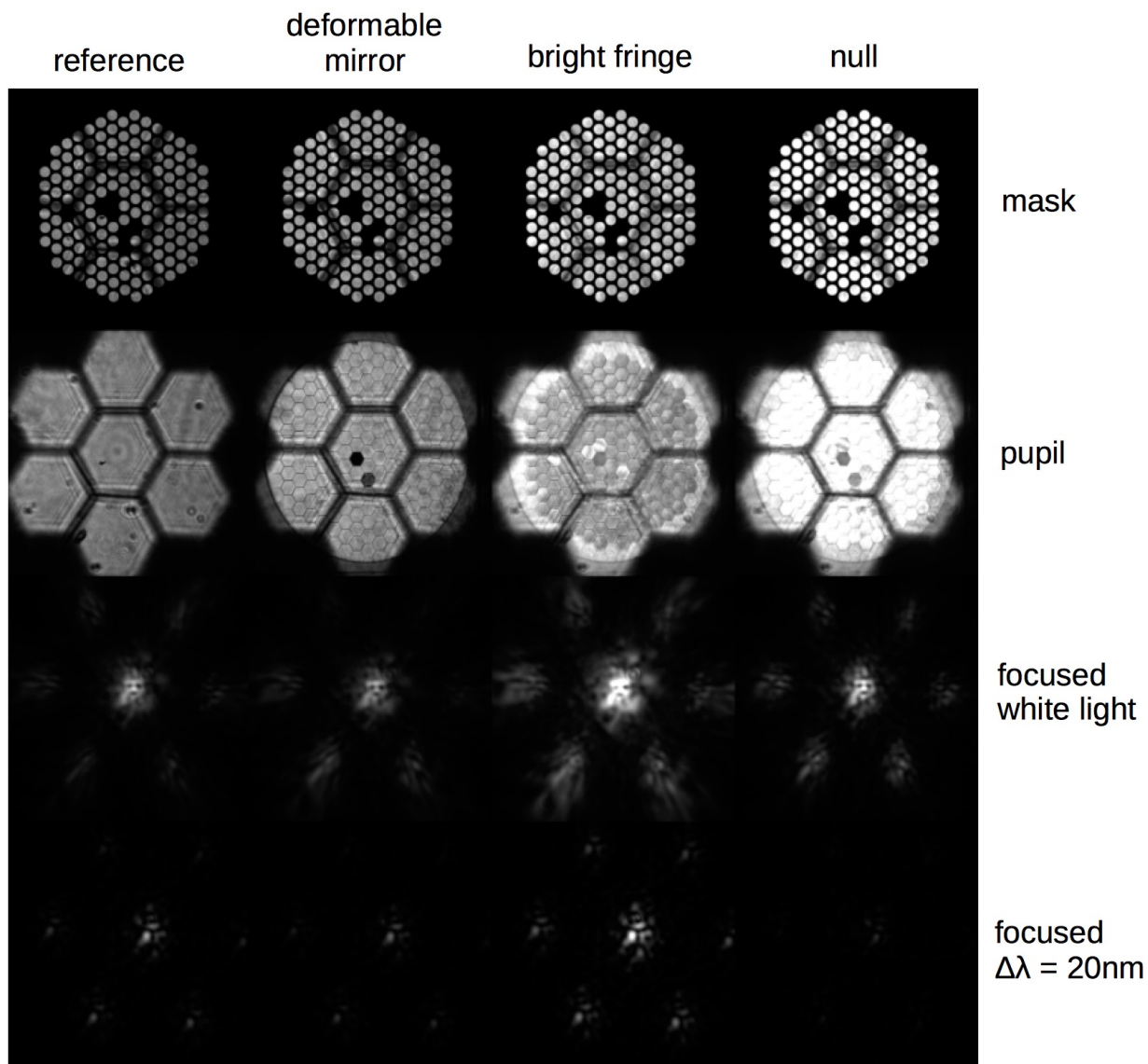


Figure 12: A matrix of imaging conditions through SAINT demonstrating basic end-to-end functionality.

the reference (delay), then deformable mirror (DM) arms of the VNC, then both shutters open with the path delay set near bright, then null fringes as observed simultaneously and antisymmetrically. The top two rows show the interferometric bright output pupil used for sensing feedback to the DM with (*top*, labeled “mask”) and without the digital mask (*below*, labeled “pupil”) applied that corresponds to the physical Lyot mask used to block out DM segmented gaps. The bright output observes white light at all times. The bottom half of the matrix shows interferometric dark output focal plane images with unfiltered light above the MS 3 $\approx 20\text{nm}$ bandpass frames. Efforts to achieve the designed magnification were left to be completed at a later date in order to do all that could be done to successfully complete MS 1.5 with remaining project schedule.

4.1 Segmented primary mirror alignment

Minimal effort was afforded to work towards closing the loop between the segmented M1 actuation and LOWFS as depicted in design and test (Fig. 13) and modeling (Fig. 14). The yet to be successfully demonstrated approach to aligning the M1 involves first adjusting three perimeter M1 segments relative to the central M1 segment in tip and tilt, then in piston while a large angular offset is applied to the remaining third segment in each of the three groups. After the first three segments are adjusted, the next three are aligned, again first in tip and tilt, then in piston. The tip and tilt correction is performed by measuring centroid separations and applying a voltage to pixel offset correction using responses measured for each of the 21 PZT actuators. Control voltage to pixel response has been coarsely measured through a manual process followed by analysis for two different sets of vertex sampling lenses of differing focal lengths.

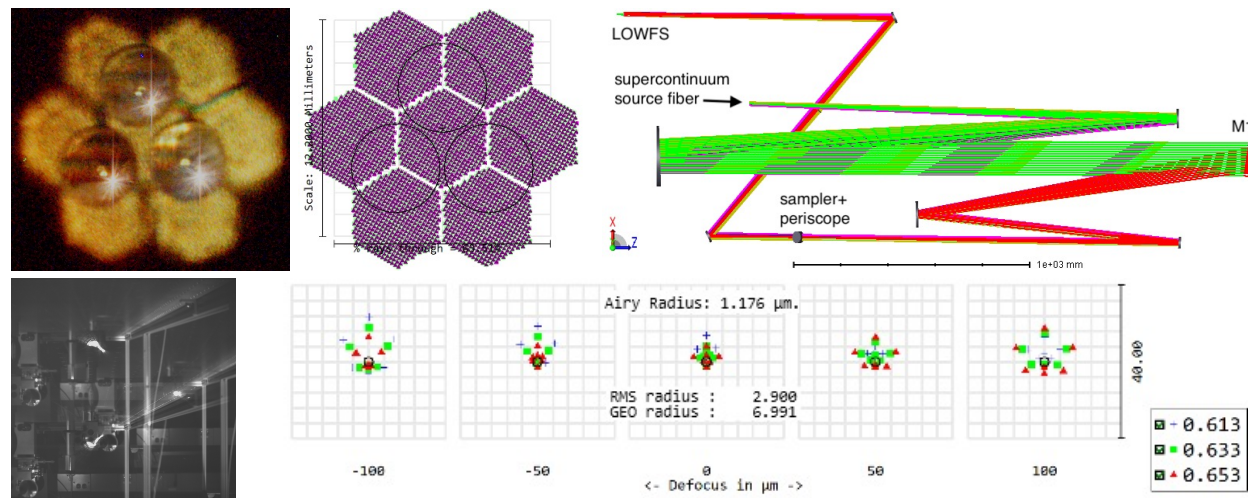


Figure 13: The MS 3 segmented primary (M1) and LOWFS subsystem. The upper left shows the SAINT M1 imaged on three 6mm diameter $f/6$ lenses that are nominally coupled to the LOWFS with a non-rotating focus mechanism. The corresponding footprint diagram corresponds to the plane where the beam color changes from red to green above the LOWFS label in the raytrace. Through focus chromatic effects are modeled for comparison with Fig. 14. An illustrative LOWFS frame is shown in the lower left; the frame was captured with the source and room lights on.

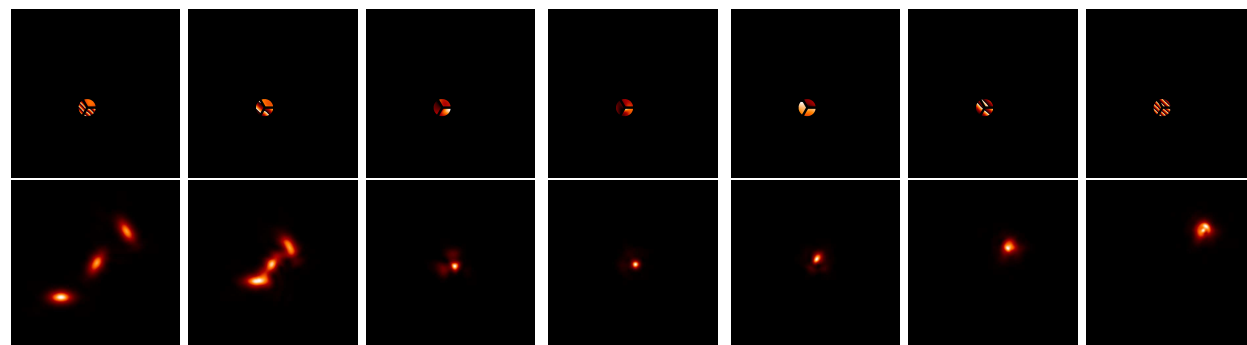


Figure 14: Modeled exit pupil tilt phase for the three segment vertices spanned by individual LOWFS lenses (*top*) and corresponding PSFs (*bottom*) for (*left to right of center*) decreasing equal but opposite amounts of diagonal tilt error relative to the central segment, and (*right to left of center*) equal amounts of diagonal tilt for all three segments. These models may be compared to the illustrative frame shown in Fig. 13 for three such groupings corresponding to each lens.

4.2 Fine Pointing System (FPS) performance

In the lab, environmental dynamical sources such as seismic vibrations, convection, and acoustics all cause beam jitter that manifest as path errors and spot motion relative to the dark region of targeted high-contrast optimization on the SCI detector. SAINT has a fine pointing system (FPS) to mitigate these disturbances. The FPS consists of a fast steering mirror (FSM) driven by closed loop spot centroid feedback sensed by an angle tracker camera (ATC). Fig. 15 contrasts pointing jitter observed on the ATC in uncontrolled and controlled states along with corresponding power spectra and time series for each state.² The FPS time series show a roughly equivalent 1s integrator settle time following the initial offset correction to the null center. Further work remains to better focus the spot on ATC and reduce its field of view to minimize centroid computation overhead and increase control bandwidth.

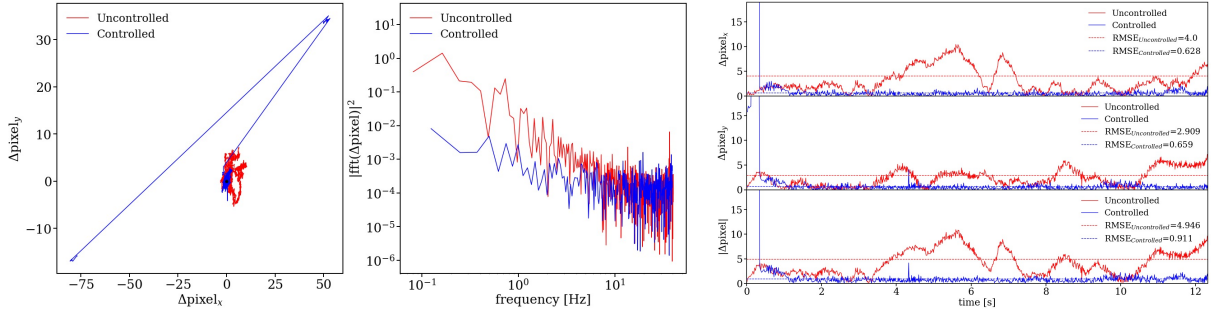


Figure 15: *Left to right*: spot jitter observed on the SAINT FPS ATC in uncontrolled and controlled states, corresponding power spectra, and time series of pixel offsets in orthogonal control directions and magnitude.

4.3 Uncontrolled telescope alignment drift and end-to-end jitter

Coarse alignment of the segmented M1 has been performed at various stages of the subsystem’s development using predominantly manual techniques. As built in the end-to-end configuration, each of the four SAINT detectors can be used to monitor M1 alignment. For example, Fig. 16 shows the M1 PSF observed on a linear scale on the ATC with two different exposure settings, τ , at approximately 80% full well, and 10τ , each captured before and after a 24-hour period where the system was left untouched following alignment. It is anticipated that a periodic PSF conditioning routine would be run to optimize the PSF quality as part of the MS 3 end-to-end high-contrast wavefront control.

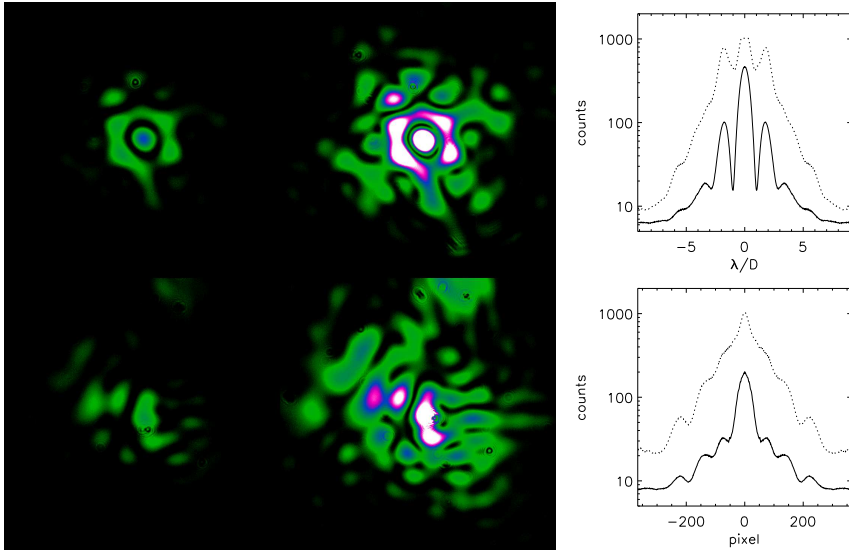


Figure 16: Images of manual alignment achieved on the SAINT M1 as observed by the ATC taken with exposure times set to τ (*left*) and 10τ (*center*), and azimuthally averaged radial intensity profiles about the centroid for each (*right*). The bottom frames and plot are the same as the top captured after leaving the system untouched for a period of 24 hours. Once aligned, the PSF observed on the ATC should best match the lower left most ASF shown in Fig. 2.

Measured pointing jitter time series and corresponding power spectra through the full SAINT end-to-end system are plotted in Fig. 17 as observed on the SCI detector without FPS stabilization presented in §4.2. In its fully operational state, the ATC is used to sense light coming directly from the telescope before being stabilized by the FSM for injection into the VNC. Comparing the SAINT end-to-end Fig. 17 with its VNC standalone Fig. 9 counterpart strengthens the case for the FPS. It is further noted that these measurements were performed with the telescope being only partially enclosed.

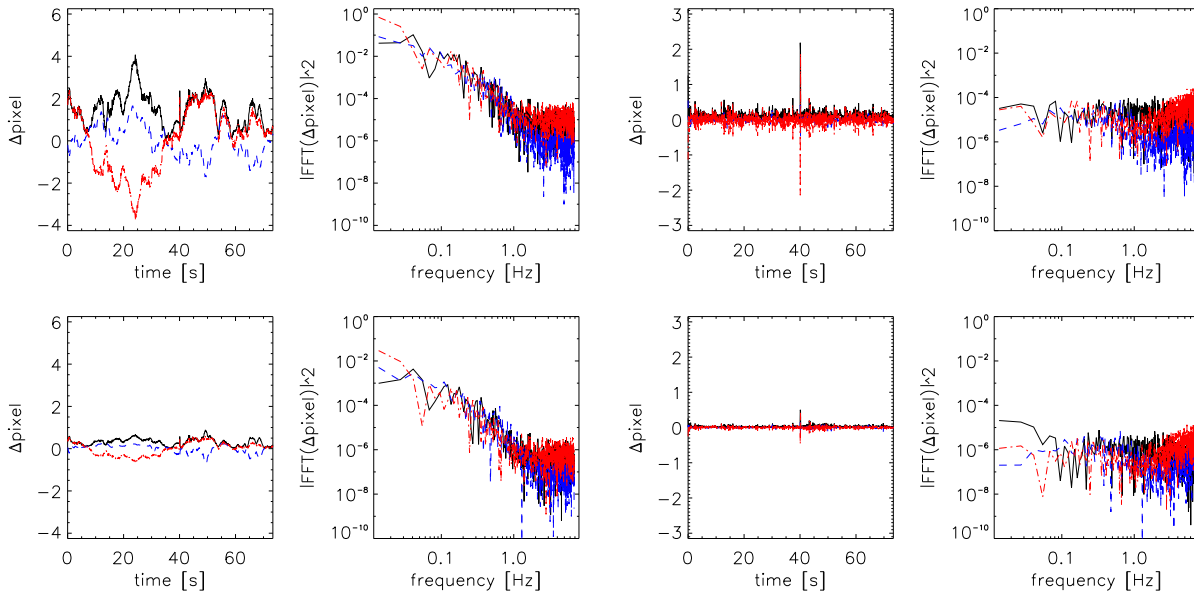


Figure 17: Similar to Fig. 9, the SAINT end-to-end interferometric centroid jitter time series and power spectra plotted for both x and y directions, as well as magnitude relative to the mean centroid location (*top*), and previous frame “instantaneous” centroid drift (*bottom*). The right plots simulate the residual error following correction with the SAINT FPS by saving frames shifted by fractional pixels determined from the first round of centroid calculations, then recalculating centroids for the shifted sets.

4.4 End-to-end operational status and next steps

The end-to-end operational status of the M1, FPS, and VNC subsystems comprising SAINT remain less than fully functional at the time of writing this report. Nonetheless, all detectors and controllers have been exercised, and closed loop control has been demonstrated on both the FPS and VNC. The system has been built and aligned to enable demonstration of basic end-to-end operation as shown in Fig. 12. The following is a list of next steps that should be taken toward completing the system assuming continued operation with the same key enabling hardware:

- Measure the interferometric stability of the VNC at low pressure
- Remove/mitigate any optical disturbances related to convection (additional variability terms of interest may be revealed, preferably not introduced)
- Hybridize beamsplitters and polarizers and their respective mounts
- Acquire and install coated Fresnel rhomb APS with simplified set and forget alignment
- Complete telescope to instrument alignment to match the as-designed magnification
- Fabricate and install an end-to-end Lyot mask to match the built as designed telescope to instrument magnification
- Complete M1 closed-loop initial alignment and alignment maintenance software

5 Summary

This NASA SAT/TDEM-13 award aimed to advance coronagraphic techniques for future segmented aperture telescopes. The SAINT system built to reach Milestone 3 consisted of a pairing of the VNC with an actively-controlled hexagonal array segmented mirror telescope via a fine pointing system. A successful VNC/SAINT SAT/TDEM-13 Milestone 3 effort was to culminate in a measurement of high-contrast source suppression with a complex aperture enabled by sequential wavefront control. This effort specifically targeted achieving a contrast of 10^{-8} over a $1\lambda/D$ diameter circular area centered at $4\lambda/D$ using a filtered source spectral bandpass of 20nm centered on 633nm. A stretch goal targeted 10^{-9} contrast at a smaller IWA, possibly $\sim 3\lambda/D$, and a broader bandpass of 40nm. These goals were not met, but the effort did succeed in advancing the segmented aperture telescope nulling concept. Prior to attempting to reach the end-to-end Milestone 3 goal, attempts at repeating Milestone 1 narrowband performance were made as Milestone 1.5. Further progress was made toward demonstrating broadband high-contrast performance for the first time as Milestone 2.5. Both Milestones 1.5 and 2.5 were to be standalone demonstrations of the VNC operating inside its vacuum chamber, independent of the air-side actively-controlled segmented telescope optics.

The Milestones were proposed as feasible objectives based on 2016 VNC Technology Readiness Levels (TRLs), and the TRL of component technologies, including wavefront sensing and control with a segmented aperture telescope, fine pointing system, deformable mirror, and delay stage. The SAINT project has furthered enabling exoplanet nulling coronagraphy with segmented aperture telescopes. Having completed this effort, additional work remains to demonstrate VNC/SAINT subsystems and components functioning in concert to meet end-to-end broadband high-contrast requirements at TRL 6. The majority of the requisite hardware and software integration has been completed and tested, demonstrations of the standalone VNC were attempted, and basic end-to-end operation through the full SAINT system was demonstrated.

Improvements since the Milestone 1 effort, most significantly, a dark channel camera with greater well-depth, introduce more heat and additional instabilities in the optical path, e.g., convection, which have not yet been eliminated. After testing the system at vacuum to measure convection's effect, it can be expected that other instabilities may remain to be identified, and potentially mitigated through modification of control laws and approach. Validation of performance requires a complete disturbance model for both our ground demonstrations, and eventually design towards a space mission. Developing a complete model turned out to be beyond the available scope, personnel, and time available to this effort. Ultimately, having not mitigated identified disturbances to achieve routine steady state operation in Milestone 1.5 as a precursor for Milestones 2.5 and 3, we cannot make useful estimates of system contrast.

Similar to any such effort, the aim of this TDEM-13 program was to achieve comprehensive success. The basic end-to-end demonstration shown in Fig. 12 evidences significant progress toward achieving this aim. While technical challenges consumed more schedule than anticipated, given added time and resources, such challenges should not be insurmountable.

Notes

¹Technical challenges that consumed more schedule than anticipated included making hardware replacements, realignment, and/or writing software to address 1) humidity damage to deformable mirrors, 2) a filter wheel that stopped functioning, and 3) troubleshoot delay stage sense and control signal electrical feedthroughs. This third item was one of several planned experiment modifications planned to reach targeted broadband and contrast performance.[12] (Tab. 4 in Appendix A lists the status of these targeted areas of improvement; it is noted that schedule associated with identifying bugs in software development, as well as designing and building the setup to measure the single mode fiber array, respectively consumed an extra several days and weeks of schedule.) Finally, an unfortunate delay in the delivery of a control computer that was specified and ordered well in advance of a planned period of development, demonstration, and optimization for the SAINT M1 closed-loop low-order wavefront sensor and controls persisted as a distraction away from priority intermediate MS efforts.

²Fig. 15 generated by Mr. Matthew Cosby, a 2018 summer intern completing a Master's in Aerospace Engineering at the University of Michigan.

Appendix A: Status of VNC TDEM-13 Whitepaper Needs

Tab. 4 presents known system issues that were identified in the VNC TDEM-10 Final Report[10]. Advances were made in all but one targeted area of improvement. All system updates noted below comprise key differences relative to the system used in the VNC TDEM-09 narrowband Milestone 1 effort. See Appendix B for additional notes on some of the components listed in Tab. 4, as well as other key similarities and differences between VNC TDEM program hardware.

Table 4: Status and recommendations for areas of improvement outlined in the TDEM-13 Whitepaper

Item	Need/Justification	Status relative to Whitepaper	Recommendations
Stable mounts	Address alignment drifts observed in TDEM-10 day-to-day efforts	COMPLETE – minimized set screw mounts and replaced zoom lenses with monolithic optics	None
Deformable mirror	Replace 97% active DM with fully functional (100% active) DM	DEGRADED – fully functional DM installed, later damaged by humidity. Ultimately using 96% active DM	Modify facilities capability and/or add humidity level margin to schedule
Delay stage	Improve coarse actuation accuracy for fringe packet scanning	COMPLETE – improved from 1-2 μ m to sub-nanometer capability	Quantify in-situ contribution to measured instabilities
Vacuum chamber	Add access ports to reduce risk and time associated with out of chamber work	COMPLETE – 11 ports added, including anti-door side to reduce adjustments requiring extraction	None
Achromatic phase shifters	Broaden high-contrast bandpass and relax alignment requirements	LIMITED PROGRESS – second set of TDEM-10 rhombs received; coated designs were advanced	Acquire, mount, and install coated APS
Control OS	Replace cumbersome and unpredictable OS with streamlined open-source platform	SIGNIFICANT PROGRESS – migrated and demonstrated legacy software; developed and tested fine pointing and primary mirror sense and control routines	Continue work towards repeating closed-loop high-contrast performance; explore active fringe tracking
Single mode fiber array	Determine possibility of demonstrating passive amplitude control with on-hand fiber arrays	COMPLETE – fiber arrays were tested and determined to be not of demonstration quality	Revisit fiber array approach viability based on future state-of-the-art quality

Appendix B: VNC TDEM-09 and TDEM-13 Hardware Comparison

In addition to Tab. 4, Tab. 5 presents the key similarities and differences between the hardware used in the successful TDEM-09 narrowband 10^{-8} contrast Milestone 1 VNC effort, and the hardware developed for TDEM-13 Milestones 1.5, 2.5, and 3.

Table 5: Key similarities and differences between VNC TDEM-09 and TDEM-13 hardware

Hardware	Similarity/Difference	Notes
Source	Similarity	Koheras/NKT SuperK Compact
Fibers	Difference	Telecom single mode cutoff models replaced with 600nm single mode cutoff fibers
Active M1 and FPS	Difference	Key to achieving end-to-end active segmented telescope nulling coronagraph demonstration objectives
Beamsplitters	Similarity	Sufficient for narrowband demonstrations, “tall pole” limitation to broadband performance
Polarizers	Difference	Matched thickness pair replaced TDEM-09 polarizers to limit chromatic wavefront error as described in §3.4
Deformable mirror	Difference	97% functional TDEM-09 unit replaced by fully functional ones that ultimately were damaged in use and subsequently replaced by best available units
Delay stage	Difference	Hybrid stepper motor + PZT actuator replaced with PiezoWalk® device
Achromatic phase shifters	Difference	Added as key enabling components for achieving broadband high-contrast performance
Wavefront sensor	Difference	Upgraded for compatibility with Linux OS
Filter wheel	Difference	Relocated from immediately following the source and before the VNC to the dark output of the VNC such that the broadest possible spectrum (shortest coherence length) is observed on the wavefront sensor at all times
Science detector	Difference	Low-noise, high dynamic range requiring fluid cooling lines installed to reach higher contrast objectives

Appendix C: TDEM-13 Subsystem Performance Summary

Tab. 6 presents required performance and measurements of subsystems and components described in this report, section by section. Notes and additional subsystem descriptions are presented along with, where applicable, limiting factors that remain to be addressed towards meeting proposed TDEM-13 objectives. It is noted that this is not an exhaustive list of all system specifications, rather a subset of the “top-level,” stressing, and/or critical requirements.

Table 6: Component and subsystem performance summary

Performance metric	Required	Measured	Section: notes, references, and limitations
Filter bandwidth ($\Delta\lambda/\lambda$)	0.10	0.048	§2.1 Radiometry: Demonstration bandpasses nominally approach what is required for exoplanet detection and characterization. Increasing source brightness to reduce exposure times and achieve more accurate control step measurements requires proportional increases in DM, delay stage, and computational bandwidths.
Throughput, source brightness driven exposure duration (τ)	< 1.0ms	\leq 2.0ms	
M1 actuator range, resolution	$\geq 5\mu\text{m}, \leq 20\text{nm}$	7 μm , NA	§2.2 Controllers and Sensors: The M1 actuators and LOWFS form the first control and sensor subsystem. The ATC and the FSM form the second control and sensor subsystem. The delay stage, DM, WFS, and dark (SCI) detector form the third and most critical control and sensor subsystem in both of the standalone VNC and full end-to-end SAINT demonstrations. Quoted dynamic range and bandwidth requirements for the WFS imply $\lambda/1000$ phase error sensitivity at 3σ significance. Increasing WFS processing bandwidth to approach the frame readout limit holds promise for both improving the starting null solution and using it as a fringe tracker for an added piston control layer in pairing with the delay stage. The dark detector dynamic range and plate scale requirements are critical to achieving sensitivity and sample statistics needed to measure the targeted MS 2.5 contrast. Quoted measured platescale and dynamic range values are determined from frame data such as that shown in Fig. 6.
LOWFS pixel size, well depth	6.5 μm , 30ke ⁻	NA	
ATC 256 \times 256 readout	\leq 2ms	1.51ms	
FSM range and bandwidth	0.5mrad, 100Hz	20mrad, NA	
Delay stage, DM control bandwidth, resolution	\geq 1kHz, \leq 1nm	NA	
WFS dynamic range, readout (frames per second)	\geq 1000, \geq 100	4096, > 400	
Dark detector dynamic range, plate scale	\geq 40ke ⁻ , \leq 0.1 $\lambda/D/\text{pix}$	\sim 43ke ⁻ , 0.076 $\lambda/D/\text{pix}$	
Source brightness stability at frequencies > 10Hz	< 0.1%	< 0.079%	§3.1 Source stability: Source brightness fluctuation through a control step measurement limits the accuracy of the measured error. In the worst case where source brightness fluctuation exceeds imparted signal variation so as to reverse the polarity of correction, the calculated solution for the controlled mode (i.e., targeted speckle within the control region of interest) will be worse than it was in the previous control step and will remain so until the next.

(continued on following page)

Tab. 6 (continued): Component and subsystem performance summary

Performance metric	Required	Measured	Section: notes, references, and limitations
Incoherent spot motion	< 0.1pix RMS	< 0.1pix RMS	§3.2 Chamber stability: High-frequency (jitter) motion measured on the dark detector for the incoherent focused spot is expected to be attributed to convection currents and mechanical perturbations. Low-frequency drift could be attributed to thermal expansion or changes in active component response, likewise as a function of temperature. Collecting data at low-pressure may help to confirm or eliminate convection as a cause of observed drifts and larger amplitude transient excursions.
RMS coherent intensity fluctuations over $(1\lambda/D)^2$ pixels	$\leq 0.025\%$	2.4%	§3.3 Nuller stability: Uncontrolled measurements were collected and analyzed for dark focal plane locations sampled near the PSF core and several λ/D off-axis. The near on-axis sample area proxies piston term measurements, i.e. path error measured between nuller arms over the full beam. The source of the significant measured drift must be identified and mitigated to close the loop on control for spatial frequencies within the targeted high-contrast region of interest.
Polarizer thickness error	< 0.1 μm	< 0.1 μm	§3.4 Broadband symmetric transmission optics measurements: Tolerances on thickness mismatches between paired optics traversed in each arm of the nuller cavity are derived from tabulated material dispersion values required to not exceed a given broadband phase error in order to meet contrast requirements. Polarizers were measured as depicted in Fig. 11. The BS/combiner pair used in the demonstration was not measured to verify performance required for MS 2.5 due to the pair being integral to the MS 1.5 effort. The quoted APS error measurement was provided by the vendor.
BS/combiner thickness error	< 0.1 μm	NA	
APS thickness error	< 0.1 μm	< 10nm	
Aligned array wavefront error	$\leq 25, 50\text{nm}$	$\leq 25\text{nm}$, NA	§4.1 Segmented primary mirror alignment: Individual segments were each polished to $\leq 25\text{nm}$ integrated RMS. The total error of the aligned array using existing hardware is approximated by the combined effects of segment figure error and alignment error attributed to limited M1 actuator resolution. The resultant $\lambda/4$ RMS ($\lambda/1.33$ P-V) PSF contains more power near the IWA than would standard optics.
Stabilized RMS jitter residual	$\leq 0.01\lambda/D$	NA	§4.2 Fine pointing system performance: The PSF location must be stabilized relative to the high-contrast region of interest. Preliminary work demonstrated a $5.4\times$ reduction in jitter relative to uncontrolled measurements.
End-to-end RMS jitter	< 0.1pix RMS	0.12pix RMS	§4.3 Uncontrolled telescope alignment drift and end-to-end jitter: Motion of the PSF should be consistent with the chamber stability (§3.2) and standalone nuller requirements (§3.3). Further work similar to that which was performed to generate Fig.16 is required to measure end-to-end PSF stability. The measurements should be performed for a coherently aligned M1 over timescales relevant to the time required to cycle through the full sequence of high-contrast wavefront control modes.
PSF stability	$\leq 0.025\%$	NA	

Appendix D: Segmented Coronagraph Design Analysis (SCDA)

Reasserting continued relevance to future missions, four sets of nulling coronagraph inputs were contributed to the SCDA[13] exoplanet yield estimation effort assuming LUVOIR 2018 Interim Report 15m obscured (on-axis) and 7.5m unobscured concept telescope apertures. Two nuller architectures were considered, the legacy dual lateral shearing VNC, and an emerging architecture that uses magnification imbalance between interfering beams to achieve a more favorable on-sky transmission pattern. Fig. 18 illustrates the apertures and nuller architectures, their associated transmission patterns, and example off-axis planet PSFs and diffracted starlight residuals associated with stellar angular diameter, which can be equated to a jittered point source. It is noted that the SAINT M1 is an off-axis design with actively controlled hexagonal segments, and adding shear to the existing VNC breadboard would produce a lab demonstration that would be most similar to what is shown for the unobscured dual lateral shear VNC exit pupil shown in Fig. 18.

Of the four configurations modeled, the on-axis LUVOIR-A legacy dual lateral shear VNC yielded the best performance with an estimated capability to detect a conservative 25 and optimistic 39 Earth-like planets in habitable zone orbits around nearby stars. Yield calculations were performed by C. Stark using the same methods as those presented in the Astro2020 Whitepaper by Stark, et al.; “Optimal Architectures and Survey Designs for Maximizing the Yields of Direct-Imaging Exoplanet Missions.” These estimates are comparable, albeit somewhat smaller, than the yields presented in the Stark, et al. Whitepaper. Given that the Whitepaper included “dozens of designs” and presents best performance among designs considered, we conclude that a VNC architecture remains of interest as the practical limitations of all architectures (including the VNC) are not yet known. The estimates include sensitivities to stellar diameter alone – jitter and low-order wavefront errors are assumed to be controlled to a negligible level relative to stellar diameter. The validity of this assumption can be checked with provided knowledge of the returned candidate targets, specifically their spectroscopic types and distances. Likewise, arbitrary levels of assumed jitter and low-order wavefront can be added to generate higher-fidelity yield estimate inputs pending the availability of resources proposed to perform such additional work.

It is understood that, within the greater SCDA effort, a head-to-head evaluation of coronagraph architectures was not performed separately. In other cases, it was assumed that a mission included a set of coronagraphs, one of which could be selected for each star given the particular angular sizes of the star and its habitable zone. The mission yield results quoted above assume a single coronagraph for each telescope, not a telescope with a selectable coronagraph. Legacy lateral VNC concepts feature mechanisms that allow for varying shear to adjust sensitivity to stellar diameter and on-sky transmission (and the laboratory VNC has this feature, but has not used it to date). Observing multiple bandpasses simultaneously is a planned LUVOIR strategy that could also be used by the VNC to increase observation efficiency towards filling in on-sky discovery space. Alternatively, the emerging radial shear nulling coronagraph could be explored to trade throughput and inner working angle for higher contrast with full discovery space in multiple spectral channels. Optimization modeling of one or both of these approaches could be included in proposed future efforts.

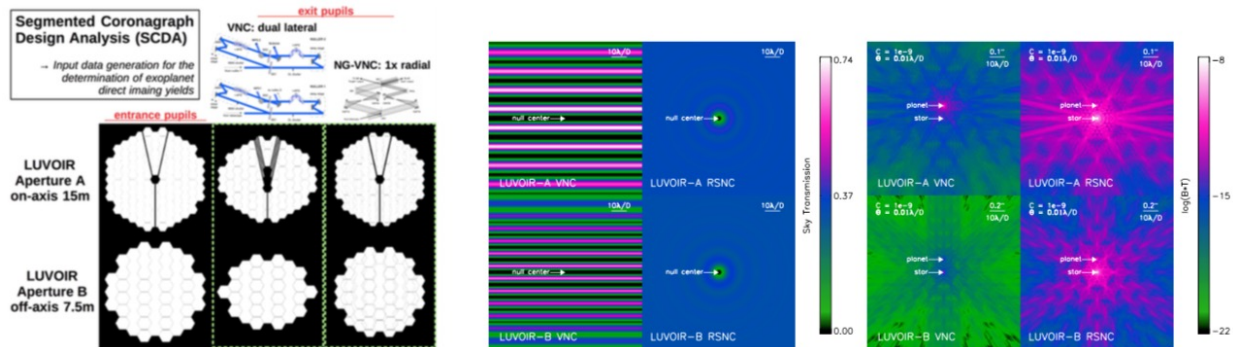


Figure 18: Entrance and exit apertures, on-sky transmission, and simulated leaked on-axis stellar and transmitted off-axis planet PSFs contributed to the SCDA exoplanet yield estimation effort.

References

- [1] Crill, B. P. and Siegler, N., “Space technology for directly imaging and characterizing exo-Earths,” *Proc. SPIE* **10398**, 103980H (Sept. 2017).
- [2] Hicks, B. A., Lyon, R. G., Petrone, P., Ballard, M., Bolcar, M. R., Bolognese, J., Clampin, M., Dogoda, P., Dworzanski, D., Helmbrecht, M. A., Koca, C., and Shiri, R., “The Segmented Aperture Interferometric Nulling Testbed (SAINT) I: overview and air-side system description,” *Proc. SPIE* **9904**, 990420 (July 2016).
- [3] Hicks, B. A., Bolcar, M. R., Helmbrecht, M. A., Petrone, P., Burke, E., Corsetti, J., Dillon, T., Lea, A., Pellicori, S., Sheets, T., Shiri, R., Agolli, J., DeVries, J., Eberhardt, A., and McCabe, T., “Segmented Aperture Interferometric Nulling Testbed (SAINT) II: component systems update,” *Proc. SPIE* **10400**, 104001I (Sept. 2017).
- [4] Hicks, B. A., Jahoda, K., Petrone, P., Sheets, T., and Boyd, P., “The segmented aperture interferometric nulling testbed (SAINT) III: control systems analysis and preliminary results,” *Proc. SPIE* **10698**, 106986M (July 2018).
- [5] Lyon, R. G., Clampin, M., Petrone, P., Mallik, U., Madison, T., and Bolcar, M. R., “High contrast vacuum nuller testbed (VNT) contrast, performance, and null control,” *Proc. SPIE* **8442** (Sept. 2012).
- [6] Clampin, M., Lyon, R., Petrone III, P., Mallik, U., Bolcar, M., Madison, T., and Helmbrecht, M., “Visible nulling coronagraph technology maturation: High contrast imaging and characterization of exoplanets,” tech. rep., NASA/Technology Development for Exoplanet Missions Final Report, JPL Document D-80950, https://exep.jpl.nasa.gov/technology/Clampin_Report_FINAL.pdf (2013).
- [7] Hicks, B., Lyon, R., Bolcar, M., Clampin, M., and Petrone, P., “High-contrast visible nulling coronagraph for segmented and arbitrary telescope apertures,” *Proc. SPIE* **9143** (2014).
- [8] Hicks, B. A., Lyon, R. G., Petrone, P., Miller, I., Bolcar, M. R., Clampin, M., Helmbrecht, M., and Mallik, U., “Demonstrating broadband billion-to-one contrast with the Visible Nulling Coronagraph,” *Proc. SPIE* **9605** (2015).
- [9] Hicks, B. A., Lyon, R. G., Petrone, P., Miller, I., Bolcar, M. R., Clampin, M., Helmbrecht, M., and Mallik, U., “Recent developments with the Visible Nulling Coronagraph,” *Proc. SPIE* **9907** (2016).
- [10] Hicks, B., Bolcar, M., Lyon, R., Clampin, M., Madison, T., Mallik, U., Petrone III, P., and Helmbrecht, M., “Technology milestone #2 final report: Achromatic visible nulling coronagraph technology maturation,” tech. rep., NASA/Technology Development for Exoplanet Missions, JPL Document D-1547413, <https://exoplanets.nasa.gov/exep/technology/TDEM-awards/> (2016).
- [11] Yaitskova, N., Dohlen, K., and Dierickx, P., “Analytical study of diffraction effects in extremely large segmented telescopes,” *J. Opt. Soc. Am. A* **20**, 1563–1575 (Aug. 2003).
- [12] Hicks, B., Bolcar, M., Petrone III, P., and Helmbrecht, M., “Technology milestone #3 whitepaper: Nulling of an actively-controlled segmented aperture telescope,” tech. rep., NASA/Technology Development for Exoplanet Missions, JPL Document D-1549543, <https://exoplanets.nasa.gov/exep/technology/TDEM-awards/> (2016).
- [13] Crill, B., Mejia Prada, C., Patterson, K., Shaklan, S., and Siegler, N., “Segmented-Aperture Coronagraphy for Exo-Earth Direct Imaging: Design and Demonstration,” in [*American Astronomical Society Meeting Abstracts #233*], *American Astronomical Society Meeting Abstracts* **233**, 326.07 (Jan. 2019).